

# Investigation of performance and stability of multilayered organometallic halide Perovskite cell

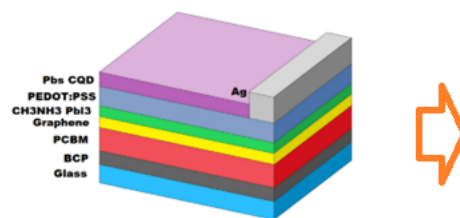
Chincholi Vishal Rudrappa,\* S. Ganesan

Department of Mechanical Engineering, Vel Tech Rangarajan Dr. Sagunthala R&D Institute of Science and Technology, Avadi, Chennai, Tamil Nadu- 600062. India.

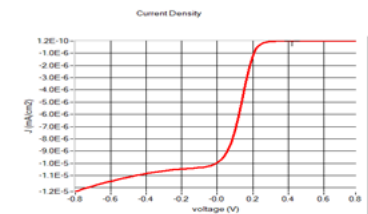
Received on: 15-Sept-2022, Accepted and Published on: 07-Nov-2022

## ABSTRACT

Perovskite solar cells (PSCs) that are organic-inorganic hybrids have received a lot of interest lately since they are extremely effective in converting power, easy manufacturing, plus minimal material costs. The hydroscopic character of organic cation, which exhibits high temperature sensitivity and makes it unsuitable for application in commercial solar panels, is primary causes of perovskite instability. The majority of previous research reported involves controlling of different solar cell material properties. The inter-transitional behavior between the layers must be considered to improve the solar cell durability. As a result, it is necessary to assess the behavior of the solar cell based on the most important simulating factors using different cell layer structures. The goal of this report is to construct and study the stability and performance of the Organo Metallic Halide Perovskite Cell while taking into account the impact of each layer on stability and effectiveness.



Designed Perovskite Cell



Performance

**Keywords:** Perovskite, Solar cells, Stability, Efficiency, Cation, Cell layer, Simulation

## INTRODUCTION

Owing to its excellent optoelectronic properties, composite natural perovskite transistors have recently emerged as the most outstanding composites for solar modules. The power conversion efficiency of perovskite solar cells have remained better due to the use of interface technology, composition technology, and processing techniques.<sup>1</sup> The benchmark efficiency values of 25.2 percent of commercial photovoltaic arrays established on silicon or inorganic thin layers have already been beaten by the newest record efficiency of 25.5 percent for perovskite solar cells.<sup>2</sup> The development of perovskite photovoltaics still faces difficulties due to the comparatively poor inherent stability of perovskites, which includes their sensitivity to moisture, oxygen, and UV light. This issue requires urgent understanding and remediation. Promising

advancements in expedited interior and exterior tests are being made as a result of growing understanding of materials and degradation mechanisms.<sup>3</sup>

The solar-powered cells utilize the perovskite materials having the molecular formula  $ABX_3$ . As opposed to B, which is an inanimate metal cation (Pb), and X, which is a halide anion ( $X = Cl, Br, \text{ or } I$ ), A is a monovalent cation (like methyl ammonium ( $CH_3NH_3$ ), MA,  $CH(NH_2)_2$  formamidinium, FA, or Cs).<sup>4</sup> Due to their outstanding physical parameters, lead-based perovskite resources are also a resurgent class of transistors.<sup>5</sup> Additionally, the mechanical strength of the solar cells within the panel affects the durability of a PV panel as well as possible power deterioration. The output power may be decreased based on the grade of cell breakdown. Because there is less active cell area when parts of the cell are electrically isolated, the cell may operate in reverse bias and be more susceptible to hot spots because of greater current densities.<sup>6</sup> Additionally,  $TiO_2$  is the ETL (Electron Transport Layer) that is most frequently employed in mesoporous p-type solar cells. This level is prone to the production of non-stoichiometry flaws like titanium interstitials and oxygen vacancies. Deep sub-band gap trap conditions are produced by these flaws, which lower solar cells' efficiency.<sup>7</sup> Spiro-OMeTAD is additionally the substance that is most frequently utilized for the hole transporting

\*Corresponding Author: Chincholi Vishal Rudrappa  
Tel: xx  
Email: Vishal.chincholi@gmail.com

Cite as: *J. Integr. Sci. Technol.*, 2023, 11(1), 465.  
URN:NBN:sciencein.jist.2023.v11.465

©Authors CC4-NC-ND, ScienceIN ISSN: 2321-4635  
<http://pubs.thesciencein.org/jist>

layer (HTL). To increase conductivity, this substance needs an addition, such as 4-tert-butylpyridine (TBP) or bis(tri-fluoromethane) sulfonimide lithium salt (Li-TFSI). However, the perovskite external is broken down by these additions, which makes the device less stable.<sup>8</sup>

Previous investigations suggested that the breakdown was not due to humidity or Ultra-Violet light, but rather metal relocation from getting closer and closer to the perovskite material. Metal wouldn't have been able to get to the perovskite absorber without the shock absorber level, which would have led to shunt channels. This hypothesis was maintained by a predicted raise in  $I_{shunt}$ , which itself is literally expressed by power supply via the metal/perovskite contact.<sup>9</sup> Additionally, encapsulation of the device would be significant for perovskite solar cells to become commercially viable because of the perovskite's propensity to disintegrate when exposed to moisture. Several teams have encapsulated tiny region devices using a crude technique at this point in the inquiry. Once the item is sliced from the roll using this procedure, exposed edges are a drawback.<sup>10</sup>

Due to their low thermal stability, organic-inorganic halide perovskites are also prone to fault development. Localized states could be produced by grain boundaries and surface flaws in perovskites and act as photo generated carrier trap centers. Therefore, these trap centers might create an arena through the substantial that would interfere with the device's total photo voltage and decrease the effectiveness.<sup>11</sup> The phenomenon of "ion migration" within the perovskite crystal organization is another key feature of PSC that may potentially affect the stability of the device. Ion movement are among the key explanations for the discontinuity kept in PSC.<sup>12</sup>

## Literature Survey

Kanoun and colleagues<sup>13</sup> tested the impact of dislocation thickness, perovskite film breadth, doping thickness, and hole transport tiers on the cell efficiency of combined cations and hydrides perovskite components in composite perovskite devices using a computational framework built on a device model. Their findings show that the optimized depth of a combined perovskite absorber is nearby 400 nm. As a result, numerous prospective inorganic hole transport levels are being studied. The outcomes display that combined perovskite with PTAA also  $Cu_2O$  as hole carrying stages were the supreme crucial factors and effective structures because to its excellent hole transport and strong power permeability.

Li and colleagues<sup>14</sup> reversed PSCs to improve their effectiveness and strength. They demonstrated that the effectiveness in addition to durability of reversed PSCs were both enhanced by functionalizing multication then halide perovskite contacts with the organometallic substance ferrocenyl-bis-thiophene-2-carboxylate (FcTc2). The FcTc2-functionalized devices similarly met the worldwide criteria for developed photovoltaics (IEC61215:2016) and showed notable durability in the damp temperature experiment (85 °C and 85 % humidity levels).

Nazim and colleagues<sup>15</sup> developed a simple and ecologically friendly synthesized strategic plan for mass production in this investigation, perovskite nanoparticles with Cr-doped hybrid

organometallic halide. In the study, methyl ammonium lead bromide,  $CH_3NH_3PbBr_3$ , was effectively doped with  $Cr^{3+}$  cations at low temperatures using an eco-friendly technique to develop crystals via anti-solvent-crystallization. The as-synthesized  $Cr^{3+}$  cation-doped perovskite nanoparticles exhibited a ~45.45% percent reduction in (100) process frequency with an improved Bragg angle ( $2\theta$ ) of  $\sim 15.01^\circ$  associated to  $\sim 14.92^\circ$  for untouched perovskites while preserving their cubic crystalline phase. To develop nanometer-sized rod-like particles, an environmentally solution, ethanol, was used as an anti-solvent during synthesis.

During PSC passivation, the electrical parameter settings of metal halide PVSK solar cells were investigated by Khan et.al.<sup>16</sup> PVSK passivation with NGQDs increases the recombination lifespan (since 31.7 to 59.9 ns), enhances interfacial charge transmission, as well as reduces trap density after  $5.531016\text{ cm}^3$  to  $4.681016\text{ cm}^3$ , as measured by photoluminescence, electrochemical impedance spectroscopy (EIS), in addition to space charge limited (SCL). The NGQDs surface enhances charge transference in the PVSK level and at the PVSK/ETL interface, that improves PSC effectiveness and is controlled by the cell's electrical characteristics.

According to Mendewala et.al.<sup>17</sup> PQDs have greater photoluminescence quantum yield than thin film counterparts as well as the additional benefit of dimension tunability, making them well-suited as LSC active media. In this paper, a simple dip-coating method for fabricating large-scale LSCs with  $CH_3NH_3PbBr_3$  (methyl ammonium lead bromide) PQDs is established, utilizing their plasmonic relationships with gold nanoparticles (AuNPs) to offset SA damages. Utilizing this AuNP-PQD coupling, 2.87 percent performance is reached in a  $100\text{ cm}^2$  LSC with a mathematical yield of 50, providing an understanding of the impact of Plasmon resonance on deposited PQDs via discharge, long life, or regionally defined photoluminescence measures.

Younes et al.<sup>18</sup> suggested [6, 6]-phenyl C61butyric acid methyl ester (PC61BM) as a popular fullerene compound engaged in electron transport level in reversed PSCs. This paper highlighted, for the first time, how to modify the characteristics of the PC61BM by doping it with fullerene C60. This doping strategy contributed to the perovskite solar cell's excellent power conversion performance of 17.46 percent versus 14.20 percent for the pristine device. All of these improvements made it possible to transfer, transport, but also gather charges more effectively while also decreasing charge recombination and interface leakage. Additionally, the improved hydrophobicity of the C60 doped PC61BM allowed enhanced ambient device stability in comparison to the unaltered gadgets. We applied our innovative technique in the ways listed below to address the issues with the current method;

- For validation, we take into account five essential stability-stimulating parameters: thickness, defect density of the absorber material, doping concentrations (ND and NA) of Electron Transport Material (ETM), and Hole Transport Material (HTM).
- An extremely thin graphene coat is applied atop the perovskite layer in order to boost performance & calculate the distinguishing traits.

## METHODS AND TECHNIQUES

The goal of this work is to design and develop the performance and reliability of the Organo Metallic Halide Perovskite Cell while examining the influence of every layer on stability and performance. The Solar Cell Capacitance Simulator (SCAPS), a software application run on a computer, is used to evaluate solar cell layout. This software tool performs and generates electrons and holes using the Poisson's and continuity formulas. In this paper, we consider five essential stability stimulating variables for validation: thickness, deficiency concentration of absorber layer, doping concentrations (ND and NA) of Electron Transport Material (ETM) and Hole Transport Material (HTM). First, a solar cell structure based on CH<sub>3</sub>NH<sub>3</sub>PbI<sub>3</sub> with PEDOT: PSS (Poly (3,4-ethylene di oxythiophene): Poly (styrene sulfonate) is an effective hole - transporting p-type absorption tier at the top and n-type PCBM (Phenyl-C61-butyric acid methyl ester) is organized at the bottom side with the greater part of electrons. The cell's reliability is then tested, and variables are acquired. Then, to increase performance, a thin graphene frame is initiated above the perovskite layer, and the features are calculated. Finally, at the bottom, a buffer layer of BCP (Bathocuproine) and Pbs colloidal quantum dots sheets is introduced, and the effectiveness and reliability are evaluated using the chosen variables. Thus, the effect of the interfacial bonding among the tiers is detected by determining the difference of effectiveness by incorporating the layers into a cell. Consequently, the research contributes to a deeper comprehension of the connecting layers within the cell. The SCAPS programme was used to identify electro-chemical properties, and Mat Lab was used to access the resulting mechanical properties. The design architecture for our proposed technique is depicted in Figure 1.

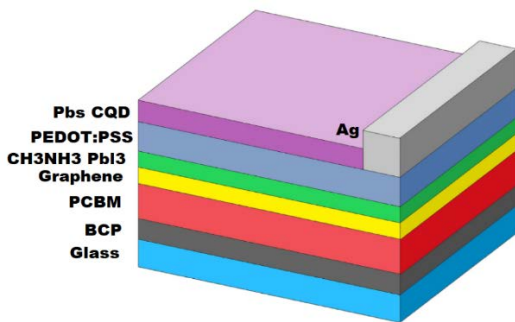


Figure 1. Architecture Design

## Layers and its properties

### Pbs CQD Layer

The presented PbS CQD solar cell is comparable to the planar hetero-junction p-i-n technique. The hole transport level assists in removing these electrons again from absorption and sending them to the electrodes. The electron transfer level is described as a path through which electrons fill the absorption level. This heterojunction structured solar panel has an interlayer, which helps to form a junction with an absorber material and focuses the most input light possible on the interfacial region as well as the absorption surface, boosting the effectiveness of the solar cell. SCAPS is used to implement the proposed PSC. The Poisson's (1) and the continuousness solutions for electrons (2) and holes (3),

correspondingly, provide the basis of this one-dimensional gadget simulation.<sup>19,20</sup>

$$\frac{d}{dx} \left( -\varepsilon(k) \frac{d\psi}{dk} \right) = q [p(k) - n(k) + M_D^+(k) - M_A^-(k) + p_t(k) - n_t(k)] \quad (1)$$

$$\frac{dp_n}{dt} = A_p - \frac{p_n - p_{no}}{\tau_p} - p_n \mu_p \frac{d\xi}{dk} - \mu_p \xi \frac{dp_n}{dk} + D_p \frac{d^2 p_n}{dk^2} \quad (2)$$

$$\frac{dn_p}{dt} = A_n - \frac{n_p - n_{po}}{\tau_n} - n_p \mu_n \frac{d\xi}{dk} - \mu_n \xi \frac{dn_p}{dk} + D_p \frac{d^2 n_p}{dk^2} \quad (3)$$

Where  $\varepsilon$  is permittivity,  $Q$  is an electron's charge,  $A$  is generation rate,  $D$  is diffusion coefficient,  $\psi$  is electrostatic potential and  $\xi$  is an electric field.  $p(y), n(y), p_t(y), n_t(y)$  are free holes, free electrons, trapped holes, and trapped electrons respectively. Ionization dopant concentration is  $M_D^+$ , and ionization donor doping concentration is  $M_A^-$ .  $k$  is the thickness and the direction.

### CH<sub>3</sub>NH<sub>3</sub>PbI<sub>3</sub>

Due to its exceptional characteristics, including its optimum band gap, broad band of absorption, excellent carrier transference device, comfort of construction on an elastic material, variable band gap, then long diffusion length,<sup>21-26</sup> CH<sub>3</sub>NH<sub>3</sub>PbI<sub>3</sub> is an outstanding bright gatherer. Initially, the maximum PCE of these PS cells constructed on CH<sub>3</sub>NH<sub>3</sub>PbI<sub>3</sub> is 3.8%.<sup>27</sup> In advance, the PCE of a perovskite solar cell reached 22.1%.<sup>28</sup> due to novel fabrication methods and the appropriate architecture selection. A typical CH<sub>3</sub>NH<sub>3</sub>PbI<sub>3</sub>-based solar cell structure includes an absorber layer, p-type PEDOT: PSS (Poly (3,4-ethylene di oxythiophene): Poly (styrene sulfonate)) at the top, as well as n-type PCBM (Phenyl-C61-butyric acid methyl ester) at the bottom. The recombination patterns, electrically charged dispersion, carrier transit procedure, and specific power density are all covered in detail by SCAPS, which also looks at the physics of the model. The electron and hole continuity formulas are:

$$\frac{dj_n}{dx} = G - R \quad (4)$$

$$\frac{dj_p}{dx} = G - R \quad (5)$$

Where,  $j_n$  is the Electron Current Density,  $j_p$  is the Hole Current Density and  $R$  is the Generation Rate. And this layer also follows the poisson equation (1) and the Drift and Diffusion Equations as follows:

$$J_n = D_n \frac{dn}{dx} + \mu_n n \frac{d\phi}{dx} \quad (6)$$

$$J_p = D_p \frac{dp}{dx} + \mu_p p \frac{d\phi}{dx} \quad (7)$$

Where  $J_n$  is Electron current density,  $D_n$  is electron diffusion coefficient,  $\mu_n$  is the electron mobility,  $J_p$  is the Hole current density and  $\mu_p$  is the Hole mobility.

### Graphene

Graphene has long been a popular nanomaterial for applications in solar cells. It has been included into the creation of several solar energy technologies, including the recently developed perovskite hybrid organic inorganic systems. In their new translucent graphite conductors for perovskite cells, Iqbal et al.<sup>29</sup> employed graphene

oxide/SnO<sub>2</sub> as the front contact on ITO. In contrast, a CH<sub>3</sub>NH<sub>3</sub>PbI<sub>3</sub> perovskite cell's interaction performance was enhanced by using hybrids of quantum dots and graphene with a performance of more than 20% which was proposed by Najafi et al.<sup>30</sup> Graphene derivations were utilized to expand the strength of perovskite cells, which are still susceptible to moisture, ion electro migration, UV, and heat decomposition. Because it enhances carriers gathering at the top cathode or lessens gadget deterioration by preventing ion electro migration from the metal electrodes to the perovskite layer, which results in electrical shunting, the graphene layer is crucial in such a hybrid device. Due to quicker temperature dissipation through the graphene surface to the atmosphere and lesser temperature produced inside the cell after actual operation, the device's thermal durability also increases. On the other hand, because graphene has poor lateral conduction, it needs to be doped with metallic ions. A high lattice imbalance will speed up

recombination, hence the intersection of graphite with a semiconductor planar substrate (like perovskite) must be properly tailored.

### BCP

The variation in energy between the highest and lowest unoccupied molecular orbitals (HOMO and LUMO) in bathocuproine (BCP), an organo transistor, is 3.5 eV.<sup>31</sup> In order to increase cell efficiency, It serves as a hole-blocking membrane among the metal cathode and also PCBM,<sup>32</sup> although it is unclear how it affects complicated aspects such the creation of an interfacial dipole film and hole conditions brought on by connection at the BCP/metal interfaces.<sup>33</sup> To predict modifications in the effectiveness of solar cells depends upon CH<sub>3</sub>NH<sub>3</sub>PbI<sub>3</sub> brought on by the BCP absorber layer situated among the PCBM as well as the metal contact. The Department of Electronics and Information Systems (ELIS) at the University of Gent created this numerical simulation programme<sup>34</sup> to examine the micro, polycrystalline, and photonic framework, define thin-film solar cell device tons of tiers with a wide range of factors, as well as overcome the basic solar cell equations: For each point, use the Poisson formula (1), the continuity equations for electrons (2), and holes (3). The effects of various densities at the interface, across the perovskite layer, fill factor (FF), short-circuit current density (Jsc), and open-circuit voltage (Voc) have also been examined.

We implemented our proposed method in a unique way based on this parameter and the values shown in table 1. The material properties such as thickness, bandgap( $E_g$ ), electron affinity( $X$ ), Dielectric permittivity ( $\epsilon$ ), mobility of electrons( $\mu_n$ ), mobility of holes( $\mu_p$ ), Carrier density of conductance band( $N_c$ ), Carrier density of valence band( $N_v$ ), Electron Thermal Velocity( $V_n$ ) and Hole Thermal Velocity( $V_p$ ).

### Mechanical Properties

In-depth research has been done on the mechanical malfunction mechanism in elastic PSCs in a number of different studies. Dong et al.<sup>35</sup> identified the impact of folding on delamination in MHP coatings using fracture mechanics studies. When a thin film is bent, it experiences compressive force within and tensile tension on the outside. The highest tensile stress is experienced when the film is bent convexly  $\sigma_T$  is given by Eq. (8)<sup>36</sup>:

$$\sigma_T = \frac{Eh}{2R} \quad (8)$$

Where E is the MHP's Young's modulus, h is the breadth of the substrate and R is the bending radius. Tensile stress causes delamination to form in MHP films. The serious tensile stress at which delamination develop can be calculated<sup>37</sup> using equation (9).

$$K = \psi \sigma_T c_0^{0.5} \geq K_{IC} = \sqrt{G_C E} \quad (9)$$

Where K denotes the stress intensity element,  $\psi$  is the geometrical constant ( $\sim \pi^{0.5}$ ),  $c_0$  represents the incident delamination's half-length (For MHP films, grain-boundary grooves & facets are still regarded as the beginning stages of delamination),  $K_{IC}$  (MPa m<sup>0.5</sup>) denotes the acute stress intensity feature of MHP for approach I delamination, and  $G_C$  (J/m<sup>2</sup>) denotes the acute strain energy release proportion. Once this condition is

**Table 1:** Layers and their properties

Parameters	CH <sub>3</sub> NH <sub>3</sub> PbI <sub>3</sub>	PCBM	BCP	PEDOT:PSS	Pbs:CQD	Graphene
Thickness	0.4 $\mu\text{m}$	0.5 $\mu\text{m}$	10nm	0.080 $\mu\text{m}$	160 nm	160 nm
Band Gap eV ( $E_g$ )	1.55	2.100	3.5	2.2	1.14	0.186
Electron affinity eV (X)	3.75	3.9	3.9	2.9	4	4.5
Dielectric permittivity $\epsilon$	6.5	3.9	4	3	2	4.17
CB effective $1/\text{cm}^3$ ( $N_c$ )	$2.2 \times 10^{15}$	$2.2 \times 10^{19}$	$2.2 \times 10^{15}$	$2.2 \times 10^{15}$	$1 \times 10^{18}$	-
VB effective $1/\text{cm}^3$ ( $N_v$ )	$2.2 \times 10^{17}$	$2.2 \times 10^{19}$	$1.8 \times 10^{17}$	$1.8 \times 10^{18}$	$1 \times 10^{19}$	-
Electron Thermal Velocity cm/S ( $V_n$ )	$1 \times 10^7$	$1 \times 10^7$	$1 \times 10^7$	$1 \times 10^7$	$2 \times 10^2$	$5.2 \times 10^7$
Hole Thermal Velocity cm/S ( $V_p$ )	$1 \times 10^7$	$1 \times 10^7$	$1 \times 10^7$	$1 \times 10^7$	$2 \times 10^{-2}$	$5 \times 10^7$
Electron mobility $\text{cm}^2/\text{V.S}$ ( $\mu_n$ )	2	0.001	0.001	0.01	$1 \times 10^{22}$	-
Hole mobility $\text{cm}^2/\text{V.S}$ ( $\mu_p$ )	2	0.002	0.002	0.0002	$1 \times 10^{22}$	-

met, i.e.,  $\sigma_T \geq (G_C E)^{0.5} / \psi c_0^{0.5}$ , an array of vertical channel delamination similar to the winding line procedures.

In equation (9), the net tensile stress should be taken into account and can be expressed as  $\sigma_{net} = \sigma_T + \sigma_R$  ( $\sigma_R > 0$  regarding tensile stiffness,  $\sigma_R < 0$  for compressive strain). Where  $\sigma_R$  is residual stress.

Substituting  $\sigma_T$  in equation (9) with equation (8), we can determine the crucial bending radius ( $R_c$ ) at which the delamination start to broadcast with equation (10).  $R_c$  would be recognised as the parameter that is most frequently used to measure the flexibility of thin films. Greater flexibility is corresponding to smaller  $R_c$ .

$$R \leq \sqrt{\frac{E}{G_C} \frac{h \psi c_0^{0.5}}{2}} = R_c \tag{10}$$

From equation (10), it is obvious that the quantity  $(E/G_C)^{1/2}$  controls the critical bending radius of thin films. As the value of  $(E/G_C)^{1/2}$  decreases, low-radius bends of thin films can be made without causing them to break.

On the other hand, the mechanical delamination of PSCs has been extensively researched. Eq. (11)<sup>38,35,39</sup> describes the delamination condition as follows:

$$G = \frac{(1 - \nu^2) t \sigma_{net}}{2E} \geq G_C \tag{11}$$

Where  $G_C$  is the rate at which the contact between the photovoltaic active element with its surrounding levels release crucial strain energy,  $\nu$  is the Poisson's ratio,  $t$  is the breadth of the thin film, then  $G$  is the rate of energy release under driving stress. According to equation (11), there are three basic ways to prevent PSC delamination: minimizing residual stress, increasing interface adhesion among the MHP level then the next level, and decreasing the thickness of the MHP film, in that order.

Additionally, interfacial delamination causes a physical separation among the MHP level and the charge carrier transport films. As an end, the fill factor (FF) with PCE decrease, and the series resistance increases.<sup>40</sup> Eq. (12)<sup>41</sup> can be used to describe the influence of series resistance also shunting resistance on the fill factor ( $FF_{sh+s}$ ).

$$FF_{sh+s} = FF_0 (1 - r_s) \left[ 1 - \frac{(v_{oc} + 0.7)}{v_{oc}} \frac{FF_0 (1 - r_s)}{r_{sh}} \right] \tag{12}$$

Where  $FF_0$  is defined as in equation(13),  $v_{oc}$  is the normalised open circuit voltage,  $r_{sh}$  is the normalised shunt resistance,  $r_s$  is the normalized series resistance,

$$FF_0 = \frac{v_{oc} - 1n(v_{oc} + 0.72)}{v_{oc} + 1} \tag{13}$$

## RESULTS AND DISCUSSION

The Solar Cell Capacitance Simulation (SCAPS) simulation was used for this programme to create and optimize the performance and reliability of the Organo Metallic Halide Perovskite Cell while assessing the impact of each layer on stability and performance.<sup>42-44</sup> A computer software called SCAPS programme created at the University of Gent using the national instrument's lab windows/CVI. The model's physics are examined using SCAPS, which also provides descriptions of the model's recombination outlines, electric field distribution, carrier transport system, as well as specific power densities. The following section explains the outcome of our proposed methodology.

## Capacitance

The capacitance value for our proposed system is presented in Figure 2. The X-axis represents voltage, while the Y-axis represents capacitance in Nano farads. The use of silver in our method, silver has high capacity to store and can produce electric current. Thus, our capacitance value increases as the frequency increases in the graph.

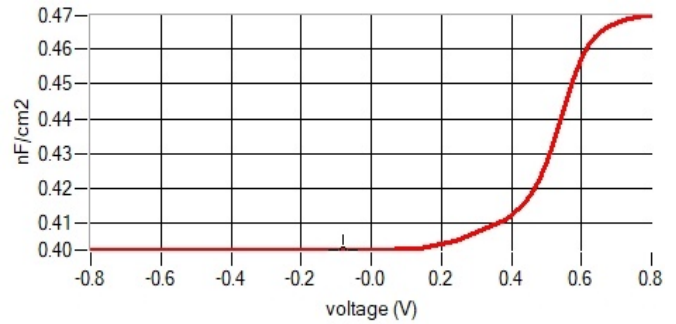


Figure 2. Capacitance

## Conductance

Figure 3 shows the conductance value for our proposed method. Since the graphene layer is used, which has high electronic conductance,<sup>45</sup> our method also benefits from high conductance. The X-axis represents voltage, and the Y-axis represents conductance in S/cm².

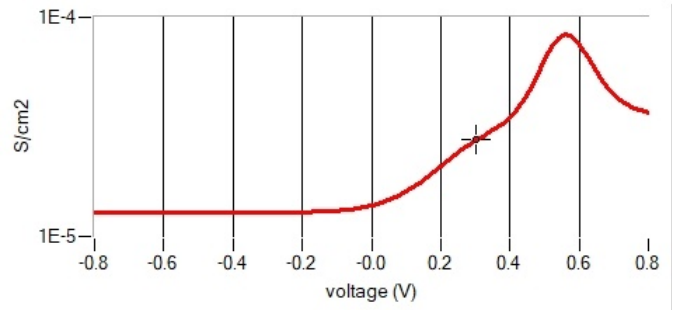


Figure 3. Conductance

## Nyquist plot

Figure 4 shows the nyquist plot for our method. A Nyquist plot is a parameterized frequency response plot that is used in automatic control and signal processing. The most primary usage of Nyquist plots is to evaluate the stability of a system with feedback.

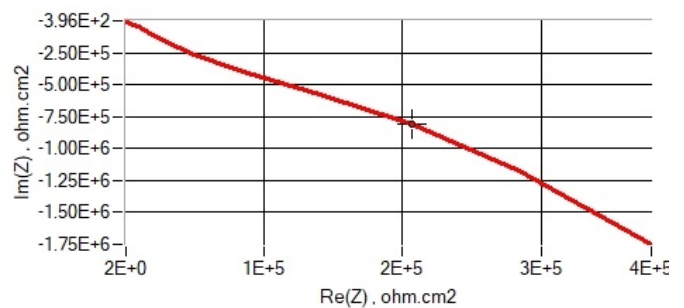


Figure 4. Nyquist plot

### Mott Schottky

Figure 5 shows the Mott Schottky plot for our method. The reciprocal of the square of capacitance ( $1/C^2$ ) is plotted beside the potential variance among the majority semiconductor then the wholesale electrolyte in the Mott-Schottky plan. Capacitance versus voltage experiments, in comparison to a typical Schottky diode, are flat around 0V.

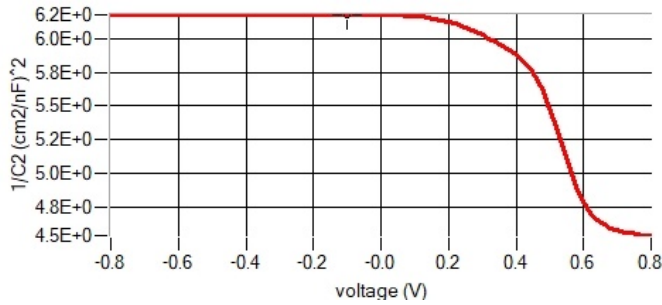


Figure 5. Mott Schottky

### Doping Profile

Figure 6 shows the doping profile for our proposed method. Doping is used to adjust the electron and hole densities because PCBM layers absorb more photon energy and produce more electron-holes. When doping is done correctly, we achieve very low energy loss and our doping increases.

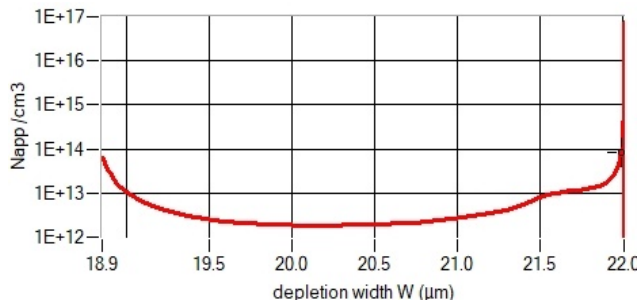


Figure 6. Doping Profile

### Current density

Figure 7 shows the current density of the proposed method. The amount of electricity that moves across a unit area of a selected cross-sections in a period of time is measured as current density.

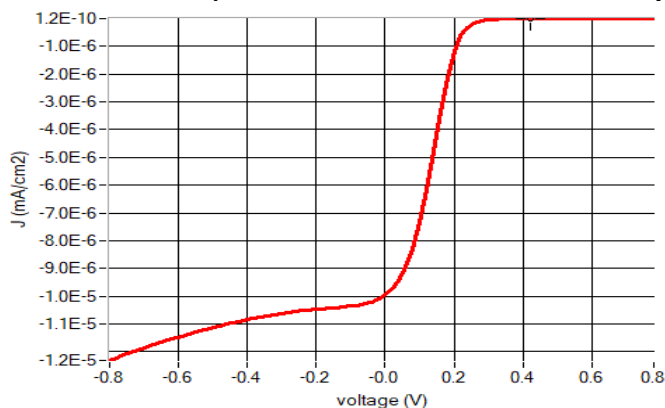


Figure 7. Current Density

The current density will be higher the more current in layers. Voltage is presented on the X-axis, and current density is displayed on the Y-axis (J-V).

### COMPARISON RESULTS

This section describes the findings of our proposed method's comparison. This section displays the thickness, generation-recombination, current density, and other parameters.

#### Thickness

The thickness of the layers used in our proposed method is depicted in Figure 8. This method employs a number of layers, including Pbs-CQD, PEDOT: PSS, CH3NH3PBI3, Graphene, PCBM, and BCP. The thickness varies as the layer changes.

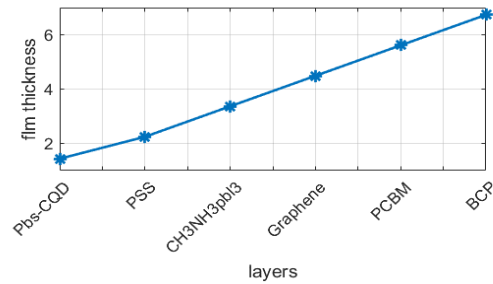


Figure 8. Thickness of layers

#### C-F Plot

Figure 9 displays the C-F plot for our proposed strategy. The Y-axis displays capacitance in nF, and the X-axis displays frequency in hertz. The level of capacitance decreases as frequency increases.

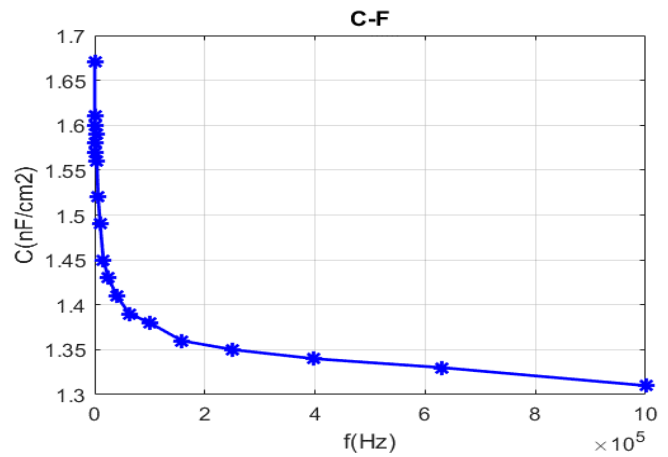


Figure 9. C-F plot

#### I-V plot

Figure 10 illustrates the current-voltage of our proposed technique. This curve displays the various ways a photovoltaic (PV) device can output current and voltage. The circuit is free of resistance, allowing the solar module to output its maximum current. Therefore, according to our proposed approach, the current charge increases as the voltage does.

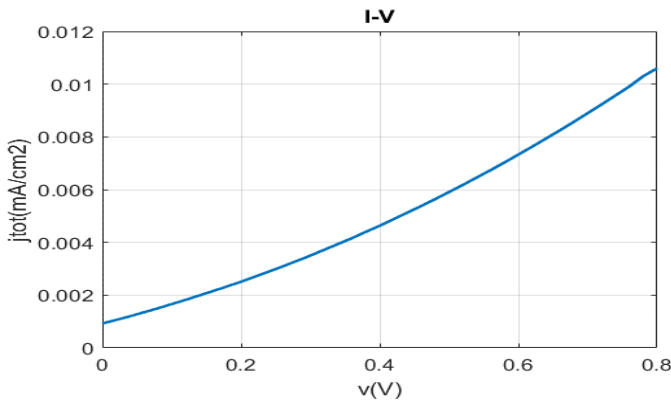


Figure 10. I-V plot

### Generation-recombination

Figure 11 shows the generation-recombination of our proposed method. In contrast to recombination, which describes how an electron in the transmission group loses power but also retakes the energy points of an electron hole in the valence band, carrier generation describes how electrons gain energy as well as transfer transitioning from a valence to the conduction band, generates two mobile operators. We gained less energy loss as a result of the doping, new materials, and electrons generated and recombined.

### Variation of parameters

Figure 12 illustrates how PV properties vary with absorber film breadth. In this diagram, the fill factor quickly decreases. The electric field has a significant impact on fill factor, and as forward bias is increased, the absorber's electric field becomes weaker. It will result in less carrier accumulation, which the electric field helped with. High fill factor requires high-quality absorber. We can infer from the Voc/thickness graph that becoming more thickness causes the Voc to decrease. According to the Jsc/thickness graph, short circuit current rises as thickness rises. This is due to the thickening process boosting the spectral sensitivity at longer wavelengths.

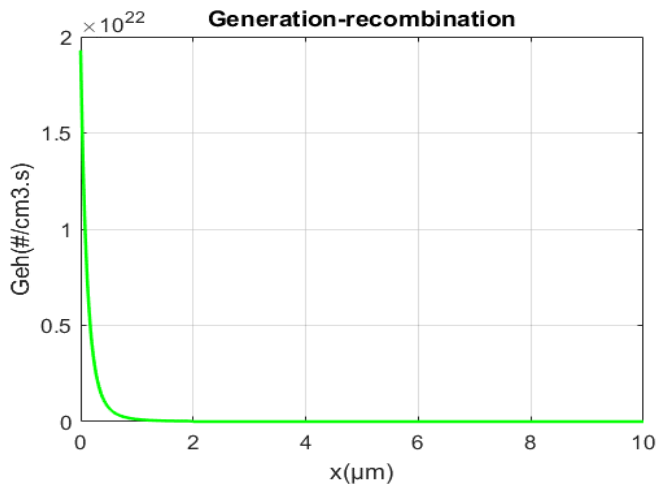


Figure 11. Generation-recombination

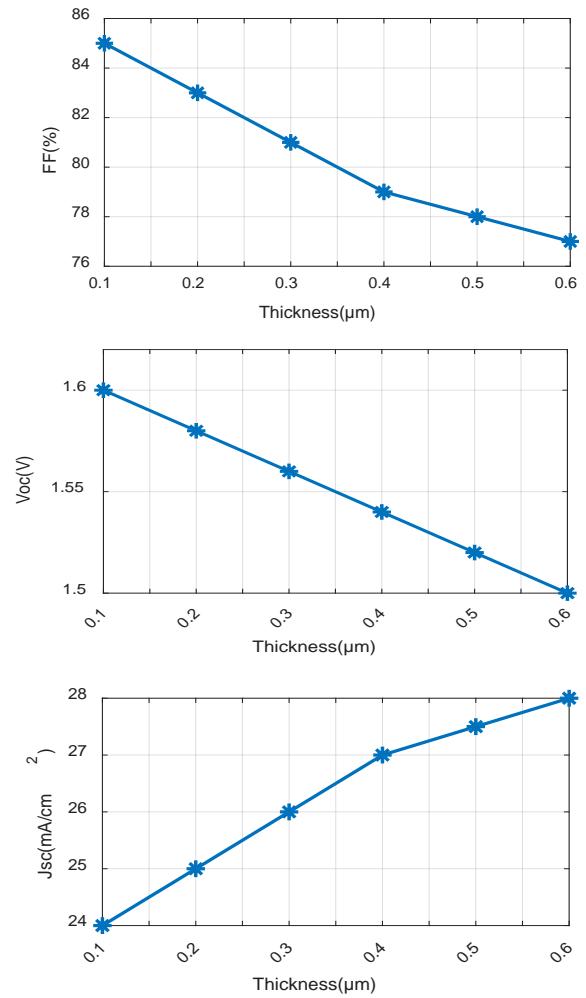
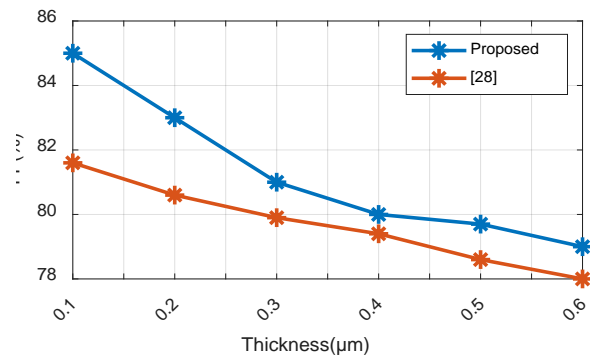


Figure 12. Variation of PV parameters by varying the thickness

### Comparison of variation of PV parameter

The comparison of PV parameter variation is shown in Figure 13. We compare our proposed strategy to [28] in this comparison graph, demonstrating that it is superior. The orange line represents the current method, and the blue line represents our proposed method. We did well in comparison of FF, Jsc, and Voc with [28].



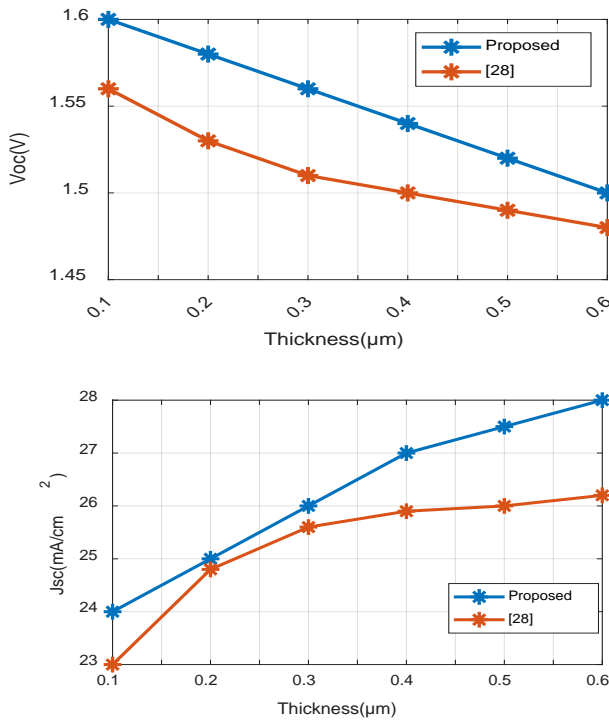


Figure 13. Comparison of variation of PV parameter

CONCLUSION

In this work, a perovskite solar cell with the following components is designed and analysed: Glass/BCP/PCBM/Graphene/CH3NH3PbI3/PEDOT: PSS/Pbs-CQD/Ag. The performance of solar cells is examined in relation to absorption tier thickness with defect density, and the impact of HTM and ETM doping concentration on PV properties is noted. Then, using the graph created by the SCAPS programme, several electrochemical properties, including those of the solar cell, were acquired. Using mathematical modelling in Matlab, the resulting values were utilized to assess mechanical factors including Young's modulus, Poisson's ratio, thickness. The effect of the interfacial interaction among the layers is spotted by determining the variation of performance by integrating the layers into a cell. The current research contributes to a deeper comprehension of the connecting layers within the cell.

CONFLICT OF INTEREST

Authors declare no conflict of interest.

NOMENCLATURE

Symbols	Description
$\epsilon$	Permittivity
$q$	charge on an electron
$A$	generation rate
$D$	diffusion coefficient
$\psi$	electrostatic potential
$\xi$	electric field
$p(y), n(y)$	free holes and free electrons
$p_t(y), n_t(y)$	both trapped electrons & holes
$M_D^+$	ionized dopant concentration

$M_A^-$	ionized acceptor doping concentration
$k$	direction & thickness together.
$j_n$	Electron Current Density
$j_p$	Hole Current Density
$R$	Generation Rate
$D_n$	electron diffusion coefficient
$D_p$	Hole diffusion coefficient
$\mu_n$	electron mobility
$\mu_p$	Hole mobility
$E_g$	bandgap
$X$	electron affinity
$N_c$	Carrier density of conductance band
$N_v$	Carrier density of valence band
$V_n$	Electron Thermal Velocity
$V_p$	Hole thermal velocity
$E$	MHP's Young's modulus
$h$	thickness of substrate
$R$	bending radius.
$K$	stress intensity factor
$\psi$	geometrical constant
$K_{IC}$	critical stress intensity factor of MHP
$G_C$	critical strain energy release rate
$c_0$	half length of the incident delamination
$\sigma_T$	Tensile stress
$\sigma_R$	Residual stress
$R_c$	critical bending radius
$G_c$	power release rate under critical strain
$\nu$	Poisson's ratio,
$t$	thickness of the thin film
$G$	driving strain energy release rate
$v_{OC}$	normalised open circuit voltage
$r_{sh}$	normalised shunt resistance
$r_s$	normalized series resistance

REFERENCES

- W. J. Xu, S. Kopyl, A. Kholkin, and J. Rocha, Hybrid organic-inorganic perovskites: Polar properties and applications. *Coordination Chemistry Reviews* **2019**, 387, 398-414.
- M. Jošt, L. Kegelmann, L. Korte, and S. Albrecht, Monolithic perovskite tandem solar cells: a review of the present status and advanced characterization methods toward 30% efficiency, *Advanced Energy Materials* **2020**, 10, 26, p. 1904102.
- W. Huang, T. Bu, F. Huang, and Y. B. Cheng, Stabilizing high efficiency perovskite solar cells with 3D-2D heterostructures, *Joule* **2020**, 4(5), 975-979.
- M. Senno, and S. Tinte, Mixed formamidinium–methylammonium lead iodide perovskite from first-principles: hydrogen-bonding impact on the electronic properties, *Physical Chemistry Chemical Physics* **2021**, 23(12), 7376-7385.
- T. Zhu, Y. Yang, and X. Gong, Recent advancements and challenges for low-toxicity perovskite materials, *ACS applied materials and interfaces* **2020**, 12(24), 26776-26811.
- X. Menga, D. Zhangb, P. Fengb, and N. Huc, Review on mechanical behavior of solar cells for building integrated photovoltaics, *renewable energy* **2021**, 15, 16.
- J. Lee, J. Kim, C. S. Kim, and S. Jo, Compact SnO2/mesoporous TiO2 bilayer electron transport layer for perovskite solar cells fabricated at low process temperature, *Nanomaterials* **2022**, 12(4), 718.
- G. Tumen-Ulzii, T. Matsushima, and C. Adachi, Mini-review on efficiency and stability of perovskite solar cells with Spiro-OMeTAD hole transport layer: recent progress and perspectives, *Energy and Fuels* **2021**, 35(23), 18915-18927.

9. A. Fakharuddin, M. Vasilopoulou, A. Soultati, M. I. Haider, J. Briscoe, V. Fotopoulos, and M. K. Nazeeruddin, Robust inorganic hole transport materials for organic and perovskite solar cells: insights into materials electronic properties and device performance, *Solar Rrl* **2021**, 5(1), 2000555.
10. J. Li, R. Xia, W. Qi, X. Zhou, J. Cheng, Y. Chen, and X. Zhang, Encapsulation of perovskite solar cells for enhanced stability: Structures, materials and characterization, *J. Power Sources* **2021**, 485, 229313.
11. K. Yao, S. Li, Z. Liu, Y. Ying, P. Dvořák, L. Fei, and D. Lei, Plasmon-induced trap filling at grain boundaries in perovskite solar cells, *Light: Science and Applications* **2021**, 10(1), 1-12.
12. M. Li, W. W. Zuo, Q. Wang, K. L. Wang, M. P. Zhuo, H. Köbler, and A. Abate, Ultrathin Nanosheets of Oxo- functionalized Graphene Inhibit the Ion Migration in Perovskite Solar Cells, *Advanced Energy Materials* **2020**, 10(4), 1902653.
13. M. B. Kanoun, A. A. Kanoun, A. E. Merad, and S. Goumri-Said, Device design optimization with interface engineering for highly efficient mixed cations and halides perovskite solar cells, *Results in Physics* **2021**, 20, 103707.
14. Z. Li, B. Li, X. Wu, S. A. Sheppard, S. Zhang, D. Gao, and Z. Zhu, Organometallic-functionalized interfaces for highly efficient inverted perovskite solar cells, *Science* **2022**, 376(6591), 416-420.
15. M. Nazim, A. A. P. Khan, F. Khan, S. K. Cho, and R. Ahmad, Insertion of metal cations into hybrid organometallic halide perovskite nanocrystals for enhanced stability: eco-friendly synthesis, lattice strain engineering, and defect chemistry studies, *Nanoscale Advances* **2022**.
16. F. Khan, M. T. Khan, S. Rehman, and F. Al-Sulaiman, Analysis of electrical parameters of pin perovskites solar cells during passivation via N-doped graphene quantum dots, *Surfaces and Interfaces* **2022**, 102066.
17. B. Mendewala, E. T. Vickers, K. Nikolaidou, A. DiBenedetto, W. G. Delmas, J. Z. Zhang, and S. Ghosh, High Efficiency Luminescent Solar Concentrator based on Organo- Metal Halide Perovskite Quantum Dots with Plasmon Enhancement, *Advanced Optical Materials* **2021**, 9(20), 2100754.
18. E. M. Younes, A. Gurung, B. Bahrami, E. M. El-Maghraby, and Q. Qiao, Enhancing efficiency and stability of inverted structure perovskite solar cells with fullerene C60 doped PC61BM electron transport layer, *Carbon* **2021**, 180, 226-236.
19. I. Alam, R. Mollick, and M. A. Ashraf, Numerical simulation of Cs<sub>2</sub>AgBiBr<sub>6</sub>-based perovskite solar cell with ZnO nanorod and P3HT as the charge transport layers, *Physica B: Condensed Matter* **2021**, 618, 413187.
20. Y. Osman, M. Fedawy, M. Abaza, and M. H. Aly, Solar cell performance enhancement with optimized CIGS absorber bandgap and buffer layer, In *Journal of Physics: Conference Series* **2020**, 1447(1), 012057.
21. Q. Dong, Y. Fang, Y. Shao, P. Mulligan, J. Qiu, L. Cao, and J. Huang, Electron-hole diffusion lengths > 175 μm in solution-grown CH<sub>3</sub>NH<sub>3</sub>PbI<sub>3</sub> single crystals, *Science* **2015**, 347(6225), 967-970.
22. Y. Chen, J. Peng, D. Su, X. Chen, and Z. Liang, Efficient and balanced charge transport revealed in planar perovskite solar cells, *ACS applied materials and interfaces* **2015**, 7(8), 4471-4475.
23. Y. C. Hsiao, T. Wu, M. Li, Q. Liu, W. Qin, and B. Hu, Fundamental physics behind high-efficiency organo-metal halide perovskite solar cells, *J. Mater. Chem. A* **2015**, 3(30), 15372-15385.
24. S. Luo, and W. A. Daoud, Recent progress in organic-inorganic halide perovskite solar cells: mechanisms and material design, *Journal of Materials Chemistry A* **2015**, 3(17), 8992-9010.
25. G. T. Mola, Enhanced photon harvesting in OPV using optical reflective surface, *Applied Physics A* **2015**, 118(2), 425-429.
26. G. Tessema, Charge transport across bulk heterojunction organic thin film, *Applied Physics A* **2012**, 106(1), 53-57.
27. A. Kojima, K. Teshima, Y. Shirai, and T. Miyasaka, Organometal halide perovskites as visible-light sensitizers for photovoltaic cells, *Journal of the american chemical society* **2009**, 131(17), 6050-6051.
28. U. Mandadapu, S. V. Vedanayakam, and K. Thyagarajan, Simulation and analysis of lead based perovskite solar cell using SCAPS-1D, *Indian J. Sci. Technol.* **2017**, 10(11), 65-72.
29. T. Iqbal, M. Haqnawaz, M. Sultan, M. B. Tahir, M. I. Khan, K. N. Riaz, and M. Rafique, Novel graphene- based transparent electrodes for perovskite solar cells, *Int. J. Energy Res.* **2018**, 42(15), 4866-4874.
30. L. Najafi, B. Taheri, B. M artin-Garcia, S. Bellani, D. Di Girolamo, A. Agresti, and F. Bonaccorso, MoS<sub>2</sub> quantum dot/graphene hybrids for advanced interface engineering of a CH<sub>3</sub>NH<sub>3</sub>PbI<sub>3</sub> perovskite solar cell with an efficiency of over 20%, *ACS nano* **2018**, 12(11), 10736-10754.
31. G. Hill, and A. Kahn, Organic semiconductor heterointerfaces containing bathocuproine, *Journal of Applied Physics* **1999**, 86(8), 4515-4519.
32. N. Shibayama, H. Kanda, T. W. Kim, H. Segawa, and S. Ito, Design of BCP buffer layer for inverted perovskite solar cells using ideal factor, *APL Materials* **2019**, 7(3), 031117.
33. T. Sakurai, S. Toyoshima, H. Kitazume, S. Masuda, H. Kato, and K. Akimoto, Influence of gap states on electrical properties at interface between bathocuproine and various types of metals, *J. Appl. Physics* **2010**, 107(4), 043707.
34. Pettersson, C. Platzer-Björkman, U. Zimmermann, and M. Edoff, Baseline model of graded-absorber Cu (In, Ga) Se<sub>2</sub> solar cells applied to cells with Zn1-xMgxO buffer layers, *Thin Solid Films* **2011**, 519(21), 7476-7480.
35. Q. Dong, M. Chen, Y. Liu, F. T. Eickemeyer, W. Zhao, Z. Dai, and Y. Shi, Flexible perovskite solar cells with simultaneously improved efficiency, operational stability, and mechanical reliability, *Joule* **2021**, 5(6), 1587-1601.
36. S. K. Yadavalli, Z. Dai, H. Zhou, Y. Zhou, and N. P. Padture, Facile healing of cracks in organic-inorganic halide perovskite thin films, *Acta Materialia* **2020**, 187, 112-121.
37. B. R. Lawn, T. R. Wilshaw, and J. R. Rice, Fracture of brittle solids (Cambridge solid state science series).
38. C. Ramirez, S. K. Yadavalli, H. F. Garces, Y. Zhou, and N. P. Padture, Thermo-mechanical behavior of organic-inorganic halide perovskites for solar cells, *Scripta Materialia* **2018**, 150, 36-41.
39. B. Freund, and S. Suresh, *Thin film materials: stress, defect formation and surface evolution*, Cambridge university press **2004**.
40. B. Qi, and J. Wang, Fill factor in organic solar cells, *Physical Chemistry Chemical Physics* **2013**, 15(23), 8972-8982.
41. M.A. Green, Solar cell fill factors: General graph and empirical expressions, *Solid State Electronics* **1981**, 24(8), 788-789.
42. A. Patsha, S. Dhara, S. Chattopadhyay, K.-H. Chen, L.-C. Chen. Optoelectronic properties of single and array of 1-D III-nitride nanostructures: An approach to light-driven device and energy resourcing, *J. Mater. Nanosci.* **2018**, 5 (1), 1-22.
43. T.V.B. Nagaveni, K.M. Mahadevan, R. Naik, T.O.S. Kumara. Synthesis of blue light emitting 5-carboxylicacid-2-arylsbstituted benzimidazoles as photosensitizers for dye-sensitized solar cells. *J. Mater. Nanosci.* **2020**, 7 (1), 24-28.
44. B. Siwach, S. Sharma, Mohan, D. Structural, optical and morphological properties of ZnO/MWCNTs nanocomposite photoanodes for Dye Sensitized Solar Cells (DSSCs) application. *J. Integr. Sci. Technol.* **2017**, 5 (1), 1-4.
45. S. Dehmiwal, M. Bahuguna. Graphene - properties, production and rising applications: A review. *J. Mater. Nanosci.* **2021**, 8 (2), 51-63.